ADVANCED MATERIALS
www.advmat.de

Al–Ge–Al Nanowire Heterostructure: From Single-Hole Quantum Dot to Josephson Effect

*Jovian Delaforce, Masiar Sistani, Roman B. G. Kramer, Minh A. Luong, Nicolas Roch, Walter M. Weber, Martien I. den Hertog, Eric Robin, Cecile Naud, Alois Lugstein, and Olivier Buisson**

Superconductor–semiconductor–superconductor heterostructures are attractive for both fundamental studies of quantum phenomena in low-dimensional hybrid systems as well as for future high-performance low power dissipating nanoelectronic and quantum devices. In this work, ultrascaled monolithic Al–Ge–Al nanowire heterostructures featuring monocrystalline Al leads and abrupt metal–semiconductor interfaces are used to probe the low-temperature transport in intrinsic Ge (i-Ge) quantum dots. In particular, demonstrating the ability to tune the Ge quantum dot device from completely insulating, through a single-hole-filling quantum dot regime, to a supercurrent regime, resembling a Josephson field effect transistor with a maximum critical current of 10 nA at a temperature of 390 mK. The realization of a Josephson field-effect transistor with high junction transparency provides a mechanism to study sub-gap transport mediated by Andreev states. The presented results reveal a promising intrinsic Ge-based architecture for hybrid superconductor–semiconductor devices for the study of Majorana zero modes and key components of quantum computing such as gatemons or gate tunable superconducting quantum interference devices.

1. Introduction

The coupling of two well-established systems, superconducting circuits and quantum dots (QDs), to create hybrid devices has conceived a new and promising domain. The amalgamation of the superconducting proximity effect of the superconducting leads and the well-defined electronic states of the QD results in mesoscopic quantum devices with broad applications and rich physics.[1] Hybrid junctions have been realized with various architectures using a wide range of materials, with significant focus on carbon nanotubes,[2,3] graphene,[4,5] or high mobility compound semiconductors such as InSb[6,7] or InAs/InP[8–11] nanowires (NWs). These research efforts continue to highlight the richness and applicability of hybrid junctions with experiments showing interesting results, beyond Coulomb blockade (CB) and tunable supercurrent, including Kondo physics, Andreev bound states (ABS), and possible signatures of Majorana fermions.[6] Extending the architecture by the possibility to modulate the QD electrostatically, hybrid systems also resemble Josephson field-effect transistors which can be integrated into quantum devices including tunable superconducting quantum interference devices (SQUIDs)[1,12] and gated superconducting qubits (gatemons) for sensing and quantum computing applications, respectively.[13]

Recently, quantum devices based on confined Ge nanostructures have seen a growth in interest due to exceptional material properties and compatibility with mature CMOS processes. In particular, due to its large hole mobility, strong spin–orbit coupling and tunable *g*-factors, Ge is promising for both spin qubit control and, specific to hybrid junctions, for the observation of Majorana zero modes which are candidates for topological quantum computing. Ge is predominantly integrated with Si in the form of Ge/Si core/shell NW junctions,[14–17] Ge/Si planar junctions,[18,19] or Ge hut wires[20] with Si caps. However, proximity-induced superconductivity in intrinsic Ge (i-Ge) channels remains elusive. This is mainly associated with the difficulty in overcoming the metal–Ge Schottky barrier which, despite forming close to the valence band due to Fermi level pinning,[21] can prevent proximity-induced supercurrent. Overcoming the Schottky barrier requires the fabrication of high-quality electrical contacts to Ge nanostructures while simultaneously reducing the gate screening effect of the leads.[22,23] This tremendous challenge has been recently overcome through intense research on the thermal diffusion of metals into semiconducting NWs.[24–26] The absence of an intermetallic

J. Delaforce, Dr. R. B. G. Kramer, Dr. N. Roch, Dr. M. I. den Hertog, Dr. C. Naud, Dr. O. Buisson
Institut NEEL UPR2940
Université Grenoble Alpes
CNRS
Grenoble 38042, France
E-mail: olivier.buisson@neel.cnrs.fr
Dr. M. Sistani, Prof. W. M. Weber, Dr. A. Lugstein
Institute of Solid State Electronics
TU Wien
Gußhausstraße 25-25a, Vienna 1040, Austria
Dr. M. A. Luong, Dr. E. Robin
Université Grenoble Alpes
CEA
IRIG-DEPHY, F-38054, Grenoble 38054, France
The ORCID identification number(s) for the author(s) of this article can be found under https://doi.org/10.1002/adma.202101989.

DOI: 10.1002/adma.202101989

phase formation and compatible diffusion rates between Al–Ge have been exploited extensively to form true metal–Ge heterostructures with abrupt interfaces[27–30] leading to the formation of self-aligned Al NWs contacting the monolithically integrated Ge QD.

In this paper, we use such monolithic and single-crystalline Al–Ge–Al NW heterostructures integrated into a back-gated field-effect device to investigate low-temperature transport of an ultrascaled i-Ge QD embedded between two superconducting Al leads. By controlling a single gate voltage, we can adjust the system to a variety of quantum transport regimes. The transport regimes of a hybrid device are defined by its dominant energy scales: the superconducting gap (Δ), the tunnel coupling (Γ), and the charging energy (E_C).[1] Most devices are limited to a single transport regime of interest depending on its characteristic energies and gate tunability, which are determined during fabrication with or without intention.[10,18] In the actual Al–Ge–Al device, Γ and E_C can be tuned via the single back gate providing access to different transport regimes in a single device. Here, we will detail the properties of the three major regimes: first, the weak coupling regime ($\Gamma = \Delta \ll E_C$) where we observe CB with large E_C, strong confinement effects, and single hole filling. Second, the intermediate coupling regime ($\Gamma \sim \Delta \sim E_C$) where superconducting sub-gap resonances appear related to resonant effects between Andreev and QD states. Finally, the strong coupling regime where the pure Ge segment exhibits proximitized superconductivity with a tunable supercurrent extending to 10 nA and remarkable channel transparencies up to 95%. The observation of supercurrent through the i-Ge segment adds monolithic Al–Ge–Al nanowire heterostructures to the field of Ge-based superconducting hybrid junctions.

2. Results and Discussion

2.1. Fabrication of Ultrascaled Al–Ge–Al NW Devices

The Al–Ge–Al NW heterostructures have been fabricated by a thermally induced exchange reaction between vapor–liquid–solid (VLS) grown single-crystalline undoped i-Ge NWs enwrapped in a 20 nm Al_2O_3-shell and lithographically defined Al contact pads (**Figure 1**a).[27,31] This technique enables the fabrication of ultrashort Ge segments contacted by self-aligned, quasi-1D, crystalline Al leads.[25,32] By this method Ge lengths as short as 10 nm are realized,[26] well beyond lithographic limitations (see the Supporting Information for details). The rodlike structure prevents the usual screening of the gate electric field due to large lithographically defined contacts and enables excellent electrostatic control of field-effect devices.

The Al–Ge–Al NW heterostructures are integrated in a back-gated field-effect transistor architecture using a heavily p-doped Si substrate with a 100 nm thick SiO_2 dielectric layer. To

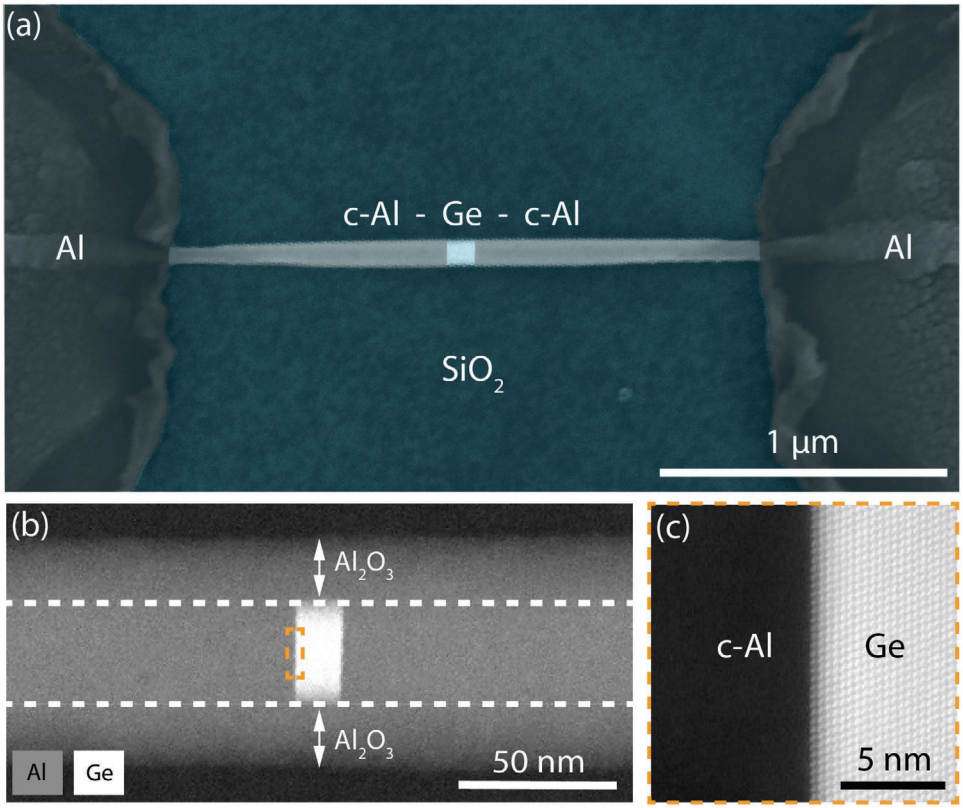

Figure 1. a) False color SEM image of an Al–Ge–Al NW heterostructure integrated in a back-gated field-effect transistor architecture. b,c) High-resolution high-angle annular dark-field (HAADF) scanning transmission electron microscopy (STEM) image using a probe-corrected FEI Titan Themis working at 200 kV of a 15 nm long Ge segment embedded in an Al–Ge–Al NW heterostructure (b) and the abrupt Al–Ge interface of the Al–Ge–Al NW heterostructure orientated along the [110] direction (c).

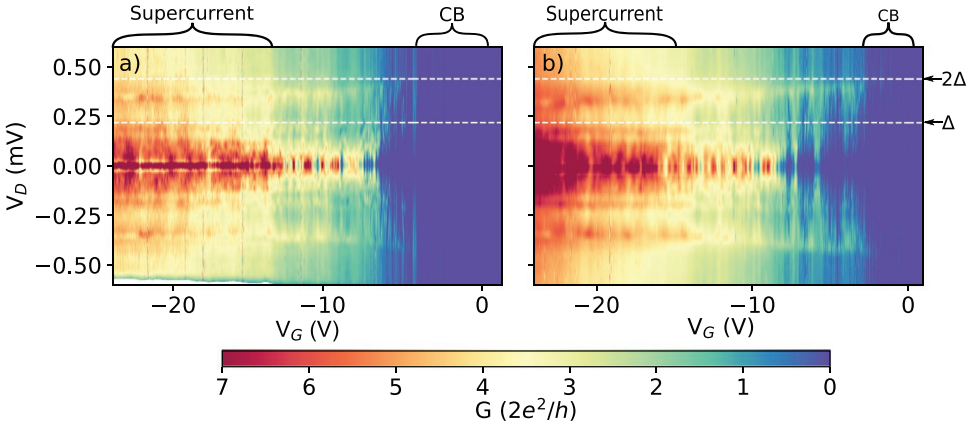

Figure 2. Density plot of differential conductance versus bias voltage (V_D) and gate voltage (V_G) of a) Sample 1 measured at 390 mK and b) Sample 2 measured at 410 mK. Four distinct regimes are observed: a full blockade regime for $V_G > 0.5$ V. A Coulomb blockade (CB) regime (-4.5 V $< V_G < 0.5$ V), labeled, an intermediate regime (-15 V $< V_G < -4.5$ V) and a supercurrent regime ($V_G < -15$ V), labeled. Horizontal dashed lines show the expected position ($eV_D = 2\Delta/n$) of the first two conductance peaks due to Andreev reflection for $\Delta = 220$ μeV.

investigate the structural properties as well as the Al–Ge interface quality, devices identical in construction have been fabricated on 40 nm thick Si_3N_4 transmission electron microscopy (TEM) membranes.[33] Figure 1b shows that the exchange reaction forms an Al–Ge–Al NW heterostructure while maintaining a uniform diameter and abrupt interface. A zoom on the Al–Ge interface (Figure 1c) reveals that the interface is nearly atomically sharp with the Ge lattice oriented along the [110] direction, transitioning to crystalline Al (c-Al) in a single atomic layer. More details regarding the principal heterostructure formation mechanism including scanning transmission electron microscopy (STEM)/energy-dispersive X-ray spectroscopy (EDX) investigations are discussed in the Supporting Information and supplied in the papers of Kral et al.[27] and El Hajraoui et al.[31]

2.2. Overview of Transport Properties

Two devices (Samples 1 and 2) have been measured with a core NW diameter of 25 nm and a Ge segment length of 42 and 37 nm, respectively. In previous work on similar devices with longer Ge segments, the room temperature mobility was estimated to be 370 $cm^2\ V^{-1}\ s^{-1}$.[34] The lower mobility of Ge NWs compared to bulk Ge is associated with their significant surface scattering.[35–37] This mobility is half of the reported mobility of 730 $cm^2\ V^{-1}\ s^{-1}$ in Ge/Si core/shell NWs with comparable diameters.[38] This higher mobility is explained by the hole gas which forms in the Ge core due to the band discontinuity between Ge and the Si shell.

Figure 2a,b shows the differential conductance, in units of quantum conductance, versus bias voltage (V_D) of Samples 1 and 2 recorded at $T = 390$ and 410 mK, respectively, over an extended gate voltage (V_G) region. The two measured devices display similar highly tunable transport properties with four distinguishable regimes: 1) a full blockade regime for $V_G > 0.5$ V, 2) a CB regime from the first hole to a few tens of holes in the QD (-4.5 V $< V_G < 0.5$ V), 3) an intermediate regime with various sub-gap features (-15 V $< V_G < -4.5$ V), and 4) a supercurrent regime at very negative gate voltages. We also observe peaks in conductance due to Andreev reflections at $eV = 2\Delta/n$, where n is the order of reflection. As discussed by Sistani et al.[29] the tunnel barriers for the actual device are defined by weak Schottky barriers for holes resulting from the combination of Fermi level pinning due to Ge surface states and band correction due to the metal/semiconductor contact. Former investigations on Al–Ge–Al heterostructures with long Ge segments[29] have shown that the gate voltage strongly modifies the valence band and Schottky barrier profile. The intrinsic coupling of the charge density and Schottky barrier enables one to simultaneously tune E_C and Γ by modulating the back gate voltage.

Comparing to estimates of the room temperature mean-free path of $\ell_{Ge} = 45$ nm[25] these devices are on the margin between the ballistic and diffusive regimes. This explains why clear quantized conductance, expected for few channel ballistic semiconductors, was not observed in the normal regime (Figure S4, Supporting Information). Given the strong similarity between the samples we will discuss these regimes hereafter using the electrical transport measurements of mainly Sample 1.

2.3. Weak Coupling Regime

Figure 3a–c shows stability diagrams of the conductance versus V_D over V_G range of -3.75 V $< V_G < 0.4$ V at 390 mK. We observe clear diamond shaped structures which points to CB suggesting that the device acts as a QD with single hole filling. Charge degeneracy points[39] occur when a charge state of the QD is in resonance with both chemical potentials of the leads allowing charge tunneling into and out of the QD. In the stability diagrams, these points manifest themselves as the juncture of the diamond edges of the N and N–1 charge states, where N is the number of holes on the QD. In Figure 3a, we observe the first charge degeneracy point at $V_G = 0.224$ V. The current pinch-off observed for $V_G > 0.274$ V and measurements up to $V_G = +5$ V revealing for both samples that current is completely blocked suggests that we are observing the introduction of the first hole in the QD at $V_G = 0.224$ V. We estimate the number

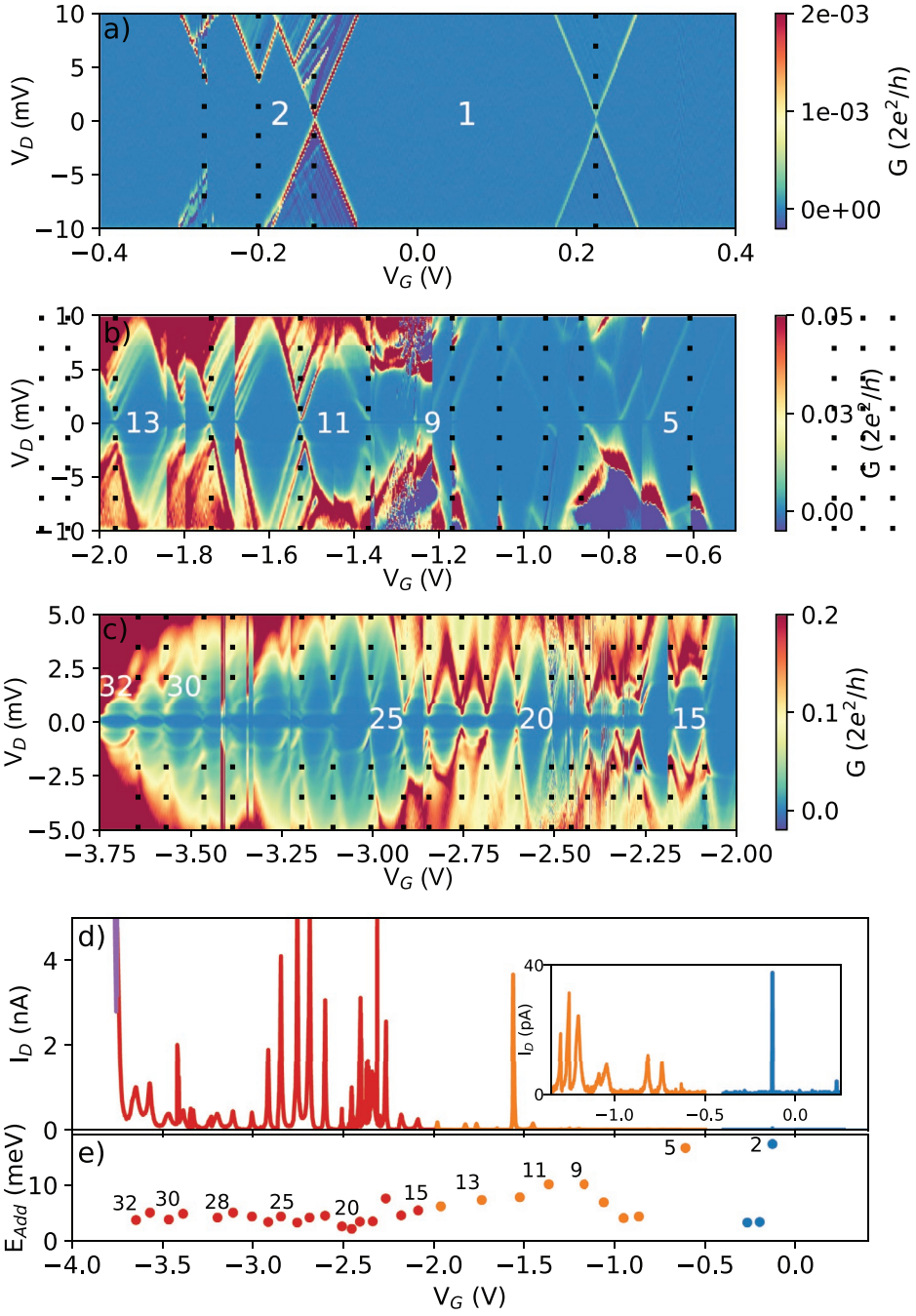

Figure 3. Stability diagram of the differential conductance (dI_D/dV_D) with respect to bias voltage (V_D) and gate voltage (V_G) in the CB regime: a) In the first hole QD regime, b) the few-hole-filling regime, c) many-hole-filling regime. The numerical labels show the estimated number of holes (N) on the quantum dot (QD) for a sample of stable charge states. The black vertical dotted lines represent the charge degeneracy points where we estimate that a new hole has been introduced to the QD, while considering the occurrence of repeated or incomplete diamonds due to charge jumps. d) I_D (V_G) slice at $V_D = 0.48$ mV. Each color represents a different measurement taken during the same cool-down (see the Supporting Information for details). (Inset) Zoom of I_D (V_G) for 0.25 V < V_G < −1.45 V. e) E_{Add}, calculated using $\alpha_G \Delta V_G$, versus V_G with sample of points labeled with the corresponding hole number (N).

of holes inside the QD by counting the number of charge degeneracy points (Figure 3). Although the occurrence of charge jumps during the measurement causes uncertainty, we estimate that this number is accurate to ±2. The presence of a superconducting gap in the density of states of the leads results in the charge degeneracy resonances occurring at non-zero bias voltages of $eV_D = \pm 2\Delta$ as clearly visible in Figure 3c. The voltage gap between the diamond peaks is ≈0.88 mV ± 0.02 mV, which

corresponds to $\Delta = 220 \pm 10$ μeV which is consistent with the observed gap in QD devices with Al contacts.[29,40] Further, the measured Δ agrees with the BCS gap of 222 μeV determined from a critical temperature of $T_C = 1.46$ K. This T_C was measured for a pure c-Al nanowire where all the Ge had diffused out of the nanowire and into the bulk Al pads.[41] Hereafter, references to the gap are associated with the superconducting gap and not the semiconducting bandgap of Ge.

We show in Figure 3d a plot of the current I_D versus V_G, by taking voltage bias slices at $V_D = 0.48$ mV (see the supporting Information for details). The plot reveals periodic current peaks separated by near-zero current regions typical of CB. Figure 3d also highlights the significant tunability of the QD's conductance: the first current peak, at $V_G = 0.224$ V, has a magnitude of ≈5 pA whereas the final current peak at $V_G = -3.645$ V has a magnitude of ≈1 nA. In the blockade regions, the current increases from 0 to 0.4 nA around $V_G = -3.6$ V. The evolution of the current can be associated with the decreasing strength of the Schottky barrier as V_G decreases. To quantify this evolution we estimate Γ (see the Supporting Information for details) for charge states $N = 2$, 17, 24, and 31 obtaining $\Gamma = 6.2$, 82, 102, and 250 μeV, respectively. Comparing to 3 meV $< E_C <$ 32 meV and $\Delta = 220$ μeV we conclude that the QD is in the weak coupling regime until $V_G \approx -3.7$ V.

Interestingly, as Γ becomes comparable to the superconducting gap ($\Gamma \sim \Delta < E_C$), a zoom on the superconducting gap reveals sub-gap conductance resonances that meet at $eV_D \approx \pm\Delta$ occur at the charge degeneracy points (see the Supporting Information). These sub-gap features are mediated by Andreev reflections and will be discussed in more detail in the next section.

Figure 3e shows the addition energy, $E_{add}(N)$, the energy required to introduce the Nth hole to the QD containing N–1 holes versus V_G. E_{add} is defined as the sum of $E_C = e^2/(C_S + C_D + C_G)$ where C_S, C_D, and C_G are the source, drain, and gate capacitances and the single particle level spacing (δ_l) which is dependent on the valence band states of the QD. The Supporting Information provides a detailed discussion of the calculation of $E_{add}(N)$. As shown in Figure 3d, in the few hole regime ($N < 10$) E_{add} is sporadic moving between 3 and 17 meV. With ≈10 holes in the QD, E_{Add} begins to decay steadily until $N \approx 20$ where it converges into an odd-even hole filling effect. From the odd–even filling effect, affirmed in the Supporting Information, the δ_l in the many-hole regime is estimated to be 1.0 ± 0.3 meV. We associate the evolution of E_{add} to the evolution of E_C already observed in long Ge segment heterostructures:[29] as V_G decreases the valence band shifts further above the Fermi energy, increasing the size of the QD, thus increasing the magnitude of C_S and C_D.

A demonstration of strong confinement in the QD is the observation of resonant tunneling through excited charge states, which manifest as conductance lines that run parallel to diamond edges. We observe such features throughout the stability diagram. From the conductance features at $V_G = -1.53$ V with $N \approx 12$, we calculate the energy of the first excited hole state to be $\Delta E = 2.0$ meV (see the Supporting Information for details). Whereas, in the many-hole regime ($N > 20$) the average energy of the observed first excited states is 1.2 ± 0.6 meV, which agrees with δ_l estimated from the odd-even effect. Using a general expression for the energy spacing due to quantum confinement $\Delta E \sim h^2/m_{eff}L^2$,[42] we coarsely estimate the effective mass (m_{eff}) to be $0.9m_e$ with m_e being the electron mass for the holes given a QD of $L = 40$ nm. This estimate is larger than the reported values of $0.28m_e$[43] for holes in Ge/Si core/shell NWs and $0.08m_e$[18] obtained from Hall measurements on SiGe/Ge/SiGe planar junctions. Further experiments and analysis are required to more accurately determine m_{eff} in our device, which are beyond the scope of this paper.

2.4. Intermediate Coupling Regime

At a gate voltage of about $V_G = -3.8$ V, CB features begin to fade out for $|V_D| > 2\Delta$. This is evident in Figure 3d where the current rapidly diverges from the periodic current peaks of the CB regime, indicating the transition to the intermediate coupling regime. In **Figure 4**b, the differential conductance versus V_D and V_G is plotted. For $V_G < -3.8$ V, sub-gap conductance peaks with periodic modulation with respect to V_G appear. These resonances forming arcs bending toward zero bias at the charge degeneracy points are interpreted as the experimental signature of single hole filling of the QD in the intermediate coupling regime. Similar to the CB regime, we estimate E_{add} (Figure 4a) and observe a continuation of the even-odd filling with comparable energies.

As the QD is filled with more holes, sub-gap features evolve; the magnitude of the conductance resonances increases and new conductance peaks emerge at lower bias voltages resulting in a reduction of the blockade region. This gate voltage dependence of the conductance peaks shows that these resonances are not simple multiple Andreev reflections (MAR) which should appear at constant bias voltage. In spectroscopy measurements performed on carbon nanotube QDs contacted by superconducting leads, such sub-gap facing bell-shaped resonances are associated with ABS which occur in a S-QD system in equilibrium through the coupling of discrete electronic states to the leads.[3]

The blue curves of Figure 4c,d show the current and the conductance as a function of the bias voltage for V_G adjusted to the degeneracy points (see vertical blue dashed line in Figure 4b). The I–V measurements reveal a current peak at a bias voltage of about –160 μeV close to $\frac{2}{3}\Delta \approx 147$ μeV. Related to this peak, negative conductance is observed in Figure 4d. Such resonances have been predicted to occur in S-QD-S systems when Γ is of the order of E_C[44] and result from the interplay between MAR resonances (the third order occurs at $V_D \approx 2/3\,\Delta$) with resonant tunneling.

Further, the resonant peak appears to be not symmetric with respect to V_D. Negative conductance shows up only at negative bias voltage and not at positive bias (blue curve). More interestingly, this asymmetry is inverted when a single hole is added inside the QD (red curve in Figure 4c,d). As previously, we observe a current and negative conductance peak but this time at positive bias voltage. In combination, these individually asymmetric curves share significant symmetry: by reflecting the red G–V_D curve about the y-axis of $V_D = 0$ V we observe the underlying symmetry between the resonance features of

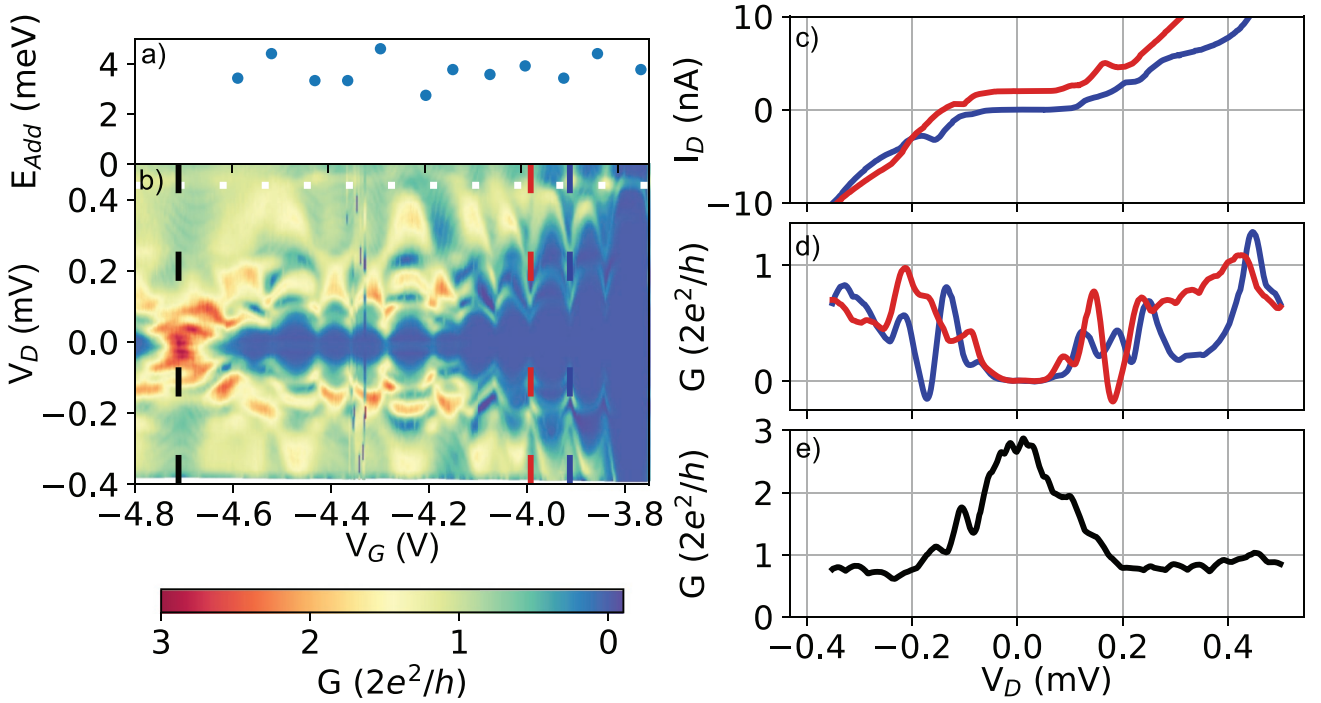

Figure 4. a) E_{Add} calculated using $\alpha_G \Delta V_G$ versus V_G. b) Density plot of differential conductance with respect to bias voltage (V_D) and gate voltage (V_G) in the intermediate regime. The white dashed line shows $eV_D = 2\Delta$ for $\Delta = 220$ μeV. We observe sub-gap conductance features that evolve with V_G. c) I_D (V_D) and d) G (V_D) slices at $V_G = -3.91$ V (dark blue) and $V_G = -3.99$ V (red). The red I_D (V_D) curve has been offset by +5 nA for clarity. e) G (V_D) curve at $V_G = -4.72$ V.

the blue and red G–V_D curves (Figure S12, Supporting Information). The intriguing symmetry between the curves of two consecutive charge degeneracy points, which is observed in both samples, needs further investigation and measurements with a magnetic field or interface gates to confirm the nature of these transport characteristics.

These sub-gap bell-shaped resonances continue until $V_G = -4.72$ V where the low voltage blockade is replaced by a zero-bias conductance peak shown in Figure 4e which we associate with superconducting transport across the QD. At lower gate voltage the intermediate regime shows regions of sub-gap features periodically separated by superconducting resonances until the supercurrent transport begins to overcome the blockade and large zero-bias conductance is observed continuously with respect to V_G marking the beginning of the supercurrent regime (Figure S11, Supporting Information).

2.5. Strong Coupling Regime

To investigate the supercurrent regime, current biasing measurements were carried out. **Figure 5**a shows a density plot of the differential resistance (dV_D/dI_D) with respect to the current bias (I_D) and V_G across the device at 390 mK. Zero dV_D/dI_D observed for a range of bias currents I_D, symmetric around $I_D = 0$, indicate dissipationless transport through the Ge segment. Figure 5b shows plots of V_D versus I_D at four gate voltages, highlighting the gate tunability and symmetry of the retrapping and critical current. For comparison, data for Sample 2 are plotted in orange. We observe gate tunable critical current up to 10 nA for Sample 1 and 6 nA for Sample 2.

Outside this dissipationless current region (Figure 5a), we observe resonant features that are continuous with respect to V_G. To further understand these features, G versus V_D curves of the same data as Figure 5b are plotted in Figure 5c. The curves reveal that the resonant features are due to bias-dependent conductance peaks, which are symmetric around a large zero-bias conductance peak corresponding to "infinite conductivity" of the supercurrent state. Further, the resonant features are consistent between Samples 1 and 2. Considering that MAR is the cause of these conductance peaks, we superimpose on Figure 5c vertical dashed lines at the expected position $V_D = \frac{2\Delta}{ne}$ with $\Delta = \Delta^* = 185$ μeV being the superconducting gap and n being the MAR order. The clear alignment of up to three MAR conductance peaks with near constant V_D positions over a large gate range and across two independently measured samples highlights the quality of these heterostructures.

Δ^* agrees with the extracted Δ from MAR in Al–Ge/Si–Al core/shell NWs that had similar Al leads,[28] however, differs significantly from the $\Delta = 220 \pm$ μeV extracted in the CB regime. This difference is understood to be due to the reduction of the superconducting gap at the Al–Ge interface resulting from the exchange of charge between the normal conductor and superconductor. This so-called inverse-proximity effect on the superconductor poisons the superconducting gap in the region that is in close proximity to the normal metal, thus reducing the magnitude of Δ,[45] which we refer to as a renormalized gap

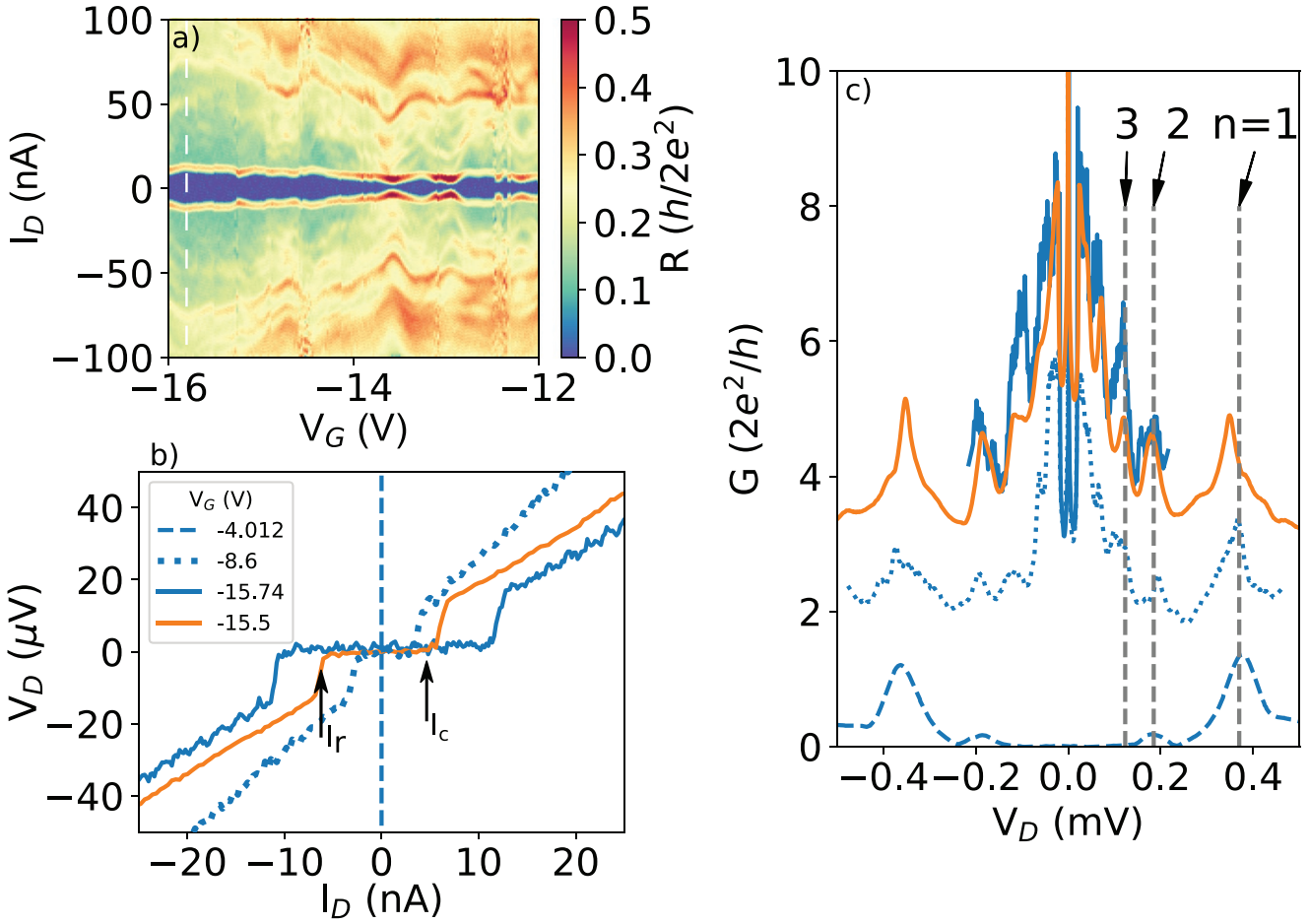

Figure 5. a) Density plot of differential resistance (dV_D/dI_D) with respect to bias current (I_D) and gate voltage (V_G) in the superconducting regime showing the gate-dependent supercurrent and MAR resonances. b) V_D versus I_D for four V_G slices showing the onset of supercurrent. For comparison both Sample 1 (blue curves) and Sample 2 are shown (orange curve). Retrapping (I_r) and critical current (I_c) are labeled. c) G (V_D) curves for the same V_G slices of (b); we see clear conductance peaks which we associate with MAR. The vertical gray dashed lines indicate the expected voltage position ($V_n = 2\Delta/ne$) of the first three MAR peaks for $\Delta = \Delta^*$ 185 μeV.

(Δ^*). The absence of the Schottky barrier in the strong coupling regime permits the inverse-proximity effect through the interaction of the QD and superconducting leads, thus resulting in the observations of a renormalised gap of Δ^* = 185 μeV, which is, as expected, less than the BCS gap.

In the weak coupling regime of our intrinsic Ge system, the strong agreement between the measured Δ = 220 μeV with the BCS gap of 222 μeV suggests there is no renormalization of the superconducting gap. Indeed in this regime the Schottky barrier at the Al–Ge interface acts as an insulating barrier isolating the QD from the superconducting leads. This isolation prevents the inverse proximity effect and thus prevents the renormalization of Δ.

The observation of MAR singularities in the supercurrent regime promotes the use of a Monte Carlo based fitting algorithm which by fitting the nonlinear I–V curves provides an estimate of the number of conduction channels and the transparency of each channel.[46] The fits of the curves of V_G = –8.6 V and V_G = –15.5 V (Figure S14, Supporting Information) provide similar high transparencies of the first channel of 95% and 96%, respectively. Consistent with the transport properties of a majority hole carrier semiconductor more conduction channels contribute to the transport at V_G = –15.5 V than V_G = –8.6 V (Figure S15, Supporting Information, for a bar chart of the respective channel transparencies). Further, the transparency of the mutually active channels (2, 3, 4) are significantly higher at V_G = –15.5 V than V_G = –8.6 V suggesting that the conduction channels are not fully open when a new channel becomes available. Nonetheless, the high transparency of the first and second channel in the case of V_G = –15.5 V endorses the high quality of these heterostructures. Such transparencies can be compared to the results of the BTK model,[47] which is often used to estimate the average contact transparency of SNS junctions. The same V_G slices –8.6 V and –15.5 V yield approximate transparencies of 60% and 90%, respectively. Though differing from the transparency results of the first channel obtained from the MAR fits, a quantitative agreement with the BTK model is obtained by taking an average of the transparencies of the first three channels, giving 60% for V_G = –8.6 V and 80% for V_G = –15.5 V.

In the ballistic regime, the superconducting coherence length of an SNS junction is given by $\xi_S = \frac{\hbar v_F}{\pi\Delta}$ where v_F is

the Fermi velocity of the semiconductor and Δ is the superconducting gap of 220 μeV. Assuming the minimum Fermi energy (E_F) of 10 meV to be the energy of the first sub-band which is estimated from the energy levels of the 1D modes in the Ge nanowire due to radial confinement[43] and a maximum effective mass of heavy holes m_{HH} of $0.28m_0$ we estimate a minimum $v_F = \sqrt{2E_F/m_{HH}}$ of 1.1×10^5 ms^{-1}. This results in a superconducting coherence length of ≈110 nm, which puts the system in the short junction limit with $L_{Ge} \ll \xi_S$. However, as $L_{Ge} \sim \ell_{Ge}$ it is difficult to define whether the junction is in the clean or dirty limit. Interestingly, the "figure-of-merit" product $I_C R_N$, where R_N is the normal resistance gives 25 μV and 16 μV for slices $V_G = -15.5$ V and $V_G = -8.6$ V respectively. For an SNS junction in the regime $L_{Ge} \ll \xi_S$ the gap is related to the $I_C R_N$ product by $eI_C R_N = \pi\Delta$. The product values are 20 and 30 times smaller than Δ suggesting that I_C is considerably suppressed possibly due to residual measurement noise and/or thermal fluctuation at $T = 390$ mK overcoming the Josephson energy $\frac{\hbar}{2e} I_c$.

3. Conclusion

We have reported on the low-temperature transport properties of monolithic Al–Ge–Al NW heterostructures with i-Ge segments of lengths of 42 and 37 nm. We have shown that the thermal exchange fabrication technique produces heterostructures with high material quality, reproducibility, and controllable Ge segments with high transparency of the Al–Ge interface (up to 96%). Using a single back gate, we can tune the system from a single-hole-filling quantum dot regime with charging energies up to 30 meV to a superconducting regime with tunable supercurrent up to 10 nA. This tunability facilitates the use of our system as a building block for the realization of a gatemon. Moreover, the subtle interplay between CB and Andreev mediated superconductivity in germanium QDs provides rich physics and a promising platform for the study of Majorana fermions. These results add further weight to the growing evidence that Ge has significant potential as a key material in future quantum technologies.

4. Experimental Section

Ge NW Synthesis: The Ge NWs were grown on Si (111) substrates using the VLS process with germane (GeH_4, 2% diluted in He) as precursor and a 2 nm thick sputtered Au layer as the 1D growth promoting catalyst. The actual growth was performed in a low pressure hot wall chemical vapor deposition chamber at 50 mbar and a gas flow of 100 sccm for both, the precursor gas and H_2 as carrier gas. After the pressure and precursor flow is stable, the temperature was ramped up at a rate of 60 K min^{-1} to the target temperature of 613 K. The rather high growth temperature ensures uniform catalyst diameter and good NW epitaxy. After a 10 min nucleation phase, the temperature is lowered to 573 K. Typical growth duration of 60 min results in 8 μm long NWs and uniform diameters of about 25 nm. Subsequently to the growth, the NWs were uniformly coated with 20 nm Al_2O_3 by atomic layer deposition.

Al–Ge–Al Device Fabrication: The starting materials are VLS grown intentionally undoped Ge NWs with a diameter of 25 nm enwrapped in a 20 nm thick Al_2O_3 passivating shell. The NWs were drop-casted onto an oxidized highly p-doped Si substrate and the Ge core NW was contacted by Al pads fabricated by electron beam lithography, 100 nm Al sputter deposition and lift-off techniques. Prior to the Al deposition a two-step wet chemical etching was performed. First, to gain access to the Ge core NW the Al_2O_3 shell was selectively removed by a 22 s dip in BHF (7%). Second, to remove the native Ge oxide layer formed underneath the Al_2O_3 shell, a 5 s HI dip (14%) was applied. The Al–Ge exchange reaction was induced by rapid thermal annealing at a temperature of $T = 674$ K in forming gas atmosphere and results in the substitution of the Ge core by c-Al.[27]

Electrical Characterization: The electrical measurements were carried out using a self-built pumped ^{3}He cryostat with a minimum temperature of $T = 340$ mK. Noise filtering was achieved using a room-temperature Pi-filter and at low temperature thermal coax of ≈1 m in length. The device was measured using a two-probe technique at low temperature using both voltage and current biasing techniques with a National Instruments PCI DAC/ADC high frequency card. The resistance of the fridge wiring was independently measured to be 390 Ω at 390 mK for which the data have been corrected for. In the voltage biasing scheme, a voltage divider consisting of 50 kΩ/50 Ω was used to reduce the amplitude of the voltage source. A Femto variable gain transimpedance amplifier (DCPCA-200) was used to convert and amplify the induced current to a voltage signal measured by the NI card. In the current biasing scheme, a 10 MΩ resistor was used to convert the voltage signal to a current signal with a maximum amplitude of 1 μA. The current was applied to the sample which was grounded at one end. The potential difference across the sample was amplified by two NF Electronic Instruments low noise preamplifiers (LI-75A), each of a gain of 100, in series. The back-gate was biased using a Yokogawa programmable voltage source. Measurements were taken with a range of bias voltages/currents, gate voltages and gains of the transimpedance amplifier. The parameters of each measurement used for discussion in the paper are detailed in the Supporting Information.

Supporting Information

Supporting Information is available from the Wiley Online Library or from the author.

Acknowledgements

J.D. and M.S. contributed equally to this work. The authors would like to acknowledge S. De Franceschi, F. Lefloch, D. Basko, K. Rafsanjani, D. Szombati, and T. Vethaak for beneficial discussions. The authors gratefully acknowledge financial support by the Austrian Science Fund (FWF): Project No. P29729-N27. The authors further thank the Center for Micro- and Nanostructures for providing the cleanroom facilities. The authors acknowledge support from the Laboratoire d'excellence LANEF in Grenoble (ANR-10-LABX-51-01). Financial support from the ANR-COSMOS (ANR-12-JS10-0002) project and ANR-QPSNWs (ANR-15-CE30-0021) project is acknowledged. The authors acknowledge support from Campus France in the framework of PHC AMADEUS 2016 for Project No. 35592PB. J. Delaforce acknowledges the European Union's Horizon 2020 research and innovation programme under the Marie Skłodowska-Curie Grant Agreement No. 754303. This project also received funding from the European Research Council under the European Union's H2020 Research and Innovation programme via the e-See project (Grant No. 758385). The authors benefitted from the access to the Nano characterization platform (PFNC) in CEA Minatec Grenoble.

Conflict of Interest

The authors declare no conflict of interest.

Data Availability Statement

The data that support the findings of this study are available from the corresponding author upon reasonable request.

Keywords

germanium, Josephson field-effect transistors, nanowire heterostructures, quantum dots, superconductor–semiconductor hybrids

Received: March 12, 2021
Revised: May 31, 2021
Published online: August 8, 2021

[1] S. De Franceschi, L. Kouwenhoven, C. Schönenberger, W. Wernsdorfer, *Nat. Nanotechnol.* **2010**, *5*, 703.
[2] A. Eichler, M. Weiss, S. Oberholzer, C. Schönenberger, A. L. Yeyati, J. C. Cuevas, A. Martín-Rodero, *Phys. Rev. Lett.* **2007**, *99*, 126602.
[3] J.-D. Pillet, C. H. L. Quay, P. Morfin, C. Bena, A. L. Yeyati, P. Joyez, *Nat. Phys.* **2010**, *6*, 965.
[4] H. B. Heersche, P. Jarillo-Herrero, J. B. Oostinga, L. M. K. Vandersypen, A. F. Morpurgo, *Nature* **2007**, *446*, 56.
[5] M. R. Sahu, X. Liu, A. K. Paul, S. Das, P. Raychaudhuri, J. K. Jain, A. Das, *Phys. Rev. Lett.* **2018**, *121*, 086809.
[6] V. Mourik, K. Zuo, S. M. Frolov, S. R. Plissard, E. P. A. M. Bakkers, L. P. Kouwenhoven, *Science* **2012**, *336*, 1003.
[7] Ö. Gül, H. Zhang, F. K. de Vries, J. van Veen, K. Zuo, V. Mourik, S. Conesa-Boj, M. P. Nowak, D. J. van Woerkom, M. Quintero-Pérez, M. C. Cassidy, A. Geresdi, S. Koelling, D. Car, S. R. Plissard, E. P. A. M. Bakkers, L. P. Kouwenhoven, *Nano Lett.* **2017**, *17*, 2690.
[8] Y.-J. Doh, J. A. van Dam, A. L. Roest, E. P. A. M. Bakkers, L. P. Kouwenhoven, S. De Franceschi, *Science* **2005**, *309*, 272.
[9] W. Chang, S. M. Albrecht, T. S. Jespersen, F. Kuemmeth, P. Krogstrup, J. Nygård, C. M. Marcus, *Nat. Nanotechnol.* **2015**, *10*, 232.
[10] K. Gharavi, G. W. Holloway, R. R. LaPierre, J. Baugh, *Nanotechnology* **2017**, *28*, 085202.
[11] L. Tosi, C. Metzger, M. F. Goffman, C. Urbina, H. Pothier, S. Park, A. L. Yeyati, J. Nygård, P. Krogstrup, *Phys. Rev. X* **2019**, *9*, 011010.
[12] M. Tinkham, *Introduction to Superconductivity*, Dover Publications, Mineola, NY, USA **2004**.
[13] T. W. Larsen, K. D. Petersson, F. Kuemmeth, T. S. Jespersen, P. Krogstrup, J. Nygård, C. M. Marcus, *Phys. Rev. Lett.* **2015**, *115*, 127001.
[14] J. Xiang, A. Vidan, M. Tinkham, R. M. Westervelt, C. M. Lieber, *Nat. Nanotechnol.* **2006**, *1*, 208.
[15] F. K. de Vries, J. Shen, R. J. Skolasinski, M. P. Nowak, D. Varjas, L. Wang, M. Wimmer, J. Ridderbos, F. A. Zwanenburg, A. Li, S. Koelling, M. A. Verheijen, E. P. A. M. Bakkers, L. P. Kouwenhoven, *Nano Lett.* **2018**, *18*, 6483.
[16] J. Ridderbos, M. Brauns, J. Shen, F. K. de Vries, A. Li, E. P. A. M. Bakkers, A. Brinkman, F. A. Zwanenburg, *Adv. Mater.* **2018**, *30*, 1802257.
[17] J. Ridderbos, M. Brauns, A. Li, E. P. A. M. Bakkers, A. Brinkman, W. G. van der Wiel, F. A. Zwanenburg, *Phys. Rev. Mater.* **2019**, *3*, 084803.
[18] N. W. Hendrickx, D. P. Franke, A. Sammak, M. Kouwenhoven, D. Sabbagh, L. Yeoh, R. Li, M. L. V. Tagliaferri, M. Virgilio, G. Capellini, G. Scappucci, M. Veldhorst, *Nat. Commun.* **2018**, *9*, 2835.
[19] F. Vigneau, R. Mizokuchi, D. C. Zanuz, X. Huang, S. Tan, R. Maurand, S. Frolov, A. Sammak, G. Scappucci, F. Lefloch, S. De Franceschi, *Nano Lett.* **2019**, *19*, 1023.
[20] H. Watzinger, C. Kloeffel, L. Vukušić, M. D. Rossell, V. Sessi, J. Kukučka, R. Kirchschlager, E. Lausecker, A. Truhlar, M. Glaser, A. Rastelli, A. Fuhrer, D. Loss, G. Katsaros, *Nano Lett.* **2016**, *16*, 6879.
[21] A. Dimoulas, P. Tsipas, A. Sotiropoulos, E. K. Evangelou, *Appl. Phys. Lett.* **2006**, *89*, 252110.
[22] A. Thanailakis, D. C. Northrop, *Solid-State Electron.* **1973**, *16*, 1383.
[23] N. Neophytou, J. Guo, M. S. Lundstrom, *IEEE Trans. Nanotechnol.* **2006**, *5*, 385.
[24] T. Burchhart, A. Lugstein, C. Zeiner, Y. J. Hyun, G. Hochleitner, E. Bertagnolli, *Elektrotech. Inftech.* **2010**, *127*, 171.
[25] M. Sistani, P. Staudinger, J. Greil, M. Holzbauer, H. Detz, E. Bertagnolli, A. Lugstein, *Nano Lett.* **2017**, *17*, 4556.
[26] M. A. Luong, E. Robin, N. Pauc, P. Gentile, M. Sistani, A. Lugstein, M. Spies, B. Fernandez, M. I. Den Hertog, *ACS Appl. Nano Mater.* **2020**, *3*, 1891.
[27] S. Kral, C. Zeiner, M. Stöger-Pollach, E. Bertagnolli, M. I. den Hertog, M. Lopez-Haro, E. Robin, K. El Hajraoui, A. Lugstein, *Nano Lett.* **2015**, *15*, 4783.
[28] M. Sistani, J. Delaforce, R. B. G. Kramer, N. Roch, M. A. Luong, M. I. den Hertog, E. Robin, J. Smoliner, J. Yao, C. M. Lieber, C. Naud, A. Lugstein, O. Buisson, *ACS Nano* **2019**, *13*, 14145.
[29] M. Sistani, J. Delaforce, K. Bharadwaj, M. Luong, J. Nacenta Mendivil, N. Roch, M. den Hertog, R. B. G. Kramer, O. Buisson, A. Lugstein, C. Naud, *Appl. Phys. Lett.* **2020**, *116*, 013105.
[30] J. Ridderbos, M. Brauns, F. K. de Vries, J. Shen, A. Li, S. Kölling, M. A. Verheijen, A. Brinkman, W. G. van der Wiel, E. P. A. M. Bakkers, F. A. Zwanenburg, *Nano Lett.* **2020**, *20*, 122.
[31] K. El hajraoui, M. A. Luong, E. Robin, F. Brunbauer, C. Zeiner, A. Lugstein, P. Gentile, J.-L. Rouvière, M. D. Hertog, *Nano Lett.* **2019**, *19*, 2897.
[32] M. A. Luong, E. Robin, N. Pauc, P. Gentile, T. Baron, B. Salem, M. Sistani, A. Lugstein, M. Spies, B. Fernandez, M. den Hertog, *ACS Appl. Nano Mater.* **2020**, *3*, 10427.
[33] M. Spies, Z. S. Momtaz, J. Lähnemann, M. Anh Luong, B. Fernandez, T. Fournier, E. Monroy, M. I. den Hertog, *Nanotechnology* **2020**, *31*, 472001.
[34] M. Sistani, P. Staudinger, A. Lugstein, *J. Phys. Chem. C* **2020**, *124*, 19858.
[35] S. Zhang, E. R. Hemesath, D. E. Perea, E. Wijaya, J. L. Lensch-Falk, L. J. Lauhon, *Nano Lett.* **2009**, *9*, 3268.
[36] R. Pillarisetty, *Nature* **2011**, *479*, 324.
[37] H. Tahini, A. Chroneos, R. W. Grimes, U. Schwingenschlögl, A. Dimoulas, *J. Phys.: Condens. Matter* **2012**, *24*, 195802.
[38] J. Xiang, W. Lu, Y. Hu, Y. Wu, H. Yan, C. M. Lieber, *Nature* **2006**, *441*, 489.
[39] R. Hanson, L. P. Kouwenhoven, J. R. Petta, S. Tarucha, L. M. K. Vandersypen, *Rev. Mod. Phys.* **2007**, *79*, 1217.
[40] G. Katsaros, P. Spathis, M. Stoffel, F. Fournel, M. Mongillo, V. Bouchiat, F. Lefloch, A. Rastelli, O. G. Schmidt, S. De Franceschi, *Nat. Nanotechnol.* **2010**, *5*, 458.
[41] F. M. Brunbauer, E. Bertagnolli, J. Majer, A. Lugstein, *Nanotechnology* **2016**, *27*, 385704.
[42] F. A. Zwanenburg, A. A. van Loon, G. A. Steele, C. E. W. M. van Rijmenam, T. Balder, Y. Fang, C. M. Lieber, L. P. Kouwenhoven, *J. Appl. Phys.* **2009**, *105*, 124314.
[43] W. Lu, J. Xiang, B. P. Timko, Y. Wu, C. M. Lieber, *Proc. Natl. Acad. Sci. USA* **2005**, *102*, 10046.
[44] A. L. Yeyati, J. C. Cuevas, A. López-Dávalos, A. Martín-Rodero, *Phys. Rev. B* **1997**, *55*, R6137.
[45] A. A. Kopasov, I. M. Khaymovich, A. S. Mel'nikov, *Beilstein J. Nanotechnol.* **2018**, *9*, 1184.
[46] J. J. Riquelme, L. de la Vega, A. L. Yeyati, N. Agraït, A. Martin-Rodero, G. Rubio-Bollinger, *Europhys. Lett.* **2005**, *70*, 663.
[47] G. E. Blonder, M. Tinkham, T. M. Klapwijk, *Phys. Rev. B* **1982**, *25*, 4515.